Engineering Failure Analysis 136 (2022) 106139

Contents lists available at ScienceDirect

Engineering Failure Analysis

journal homepage: www.elsevier.com/locate/engfailanal

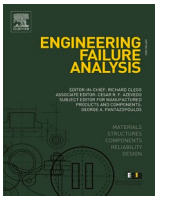

Blade thickness effects on viscous flutter in a radial turbocharger turbine

Azadeh Sajedin [a,*], John Allport [a], Mohammadreza Amoozgar [b], Omid Farhangiyan Marandi [c]

[a] Turbocharger Research Group, University of Huddersfield, Queensgate, Huddersfield HDI 3DH, United Kingdom
[b] Department of Mechanical, Materials and Manufacturing Engineering, University of Nottingham, Nottingham, NG7 2RD, United Kingdom
[c] Institute for Innovation in Sustainable Engineering, College of Science and Engineering, University of Derby, Derby DE22 1GB, United Kingdom

ARTICLE INFO

Keywords:
Flutter
Aeroelastic instability
Fourier Transformation
Turbocharger turbine
Aerodynamic damping

ABSTRACT

Transient blade loading limits the lifetime of turbocharger turbine blades. This study investigates the flutter instability of a radial turbocharger turbine blade under pulsating inlet conditions. The viscous Navier-Stokes equations with the SST-kω turbulence model and curvature correction were solved. A time-marching 3D finite volume method was used in the CFX17 CFD solver to model the vibrating blade in a traveling wave mode applying Fourier Transformation. For flutter calculations, moving boundaries with specified modal displacements were used. An area of instability was recognized on the suction-side of the rotor blade. FSI steady-state analysis was then performed to assess the effects of shock position and blade profile on the blade stability in the recognized vulnerable region. The results show that a higher trailing edge radius increases the stability and leads to a significant reduction of flutter risk whereas the maximum thickness and leading-edge radius do not notably affect the flutter occurrences.

1. Introduction

Flutter is one of the most serious aeroelastic instability problems which results in undesired vibrations of the blades of turbomachines. The flutter is produced from a balance between the unsteady forcing by fluid, and inertial damping forces and the elastic forces of the structure [1]. Under unsteady conditions, the amplitude of oscillations in each vibration cycle are multiplied by aerodynamic forces, so the amplitude can grow rapidly which in turn might result in blade failure through high cycle fatigue. Flutter is a serious problem in turbomachinery field because of features which are not fully understood such as: flow distortions due to blade-rows, assembly modal coupling, and loss of uniform vibration in wheel due to aerodynamic effects and mistuning [2]. Srinivasan [3] presented an overview of this mistuning phenomenon by including the available experimental results and the various numerical models available in the literature. The literature shows that mistuning is not a standard feature of rotor design, but it is exploited to redesign flutter-prone rotors. In parallel, experimental studies for susceptibility of rotors to flutter by combining unsteady aerodynamic pressure acting on vibration cascades has enabled prediction of aerodynamic damping. Similar results have been obtained from calculation of the resonant response of blades, but the research is not matured to the point where it can be considered in the design of systems and sustained research and development in this area is needed.

* Corresponding author at: Researcher in the Turbocharger Research Group, University of Huddersfield, United Kingdom.
E-mail address: a.sajedin@hud.ac.uk (A. Sajedin).

https://doi.org/10.1016/j.engfailanal.2022.106139
Received 16 September 2021; Received in revised form 20 January 2022; Accepted 7 February 2022
Available online 9 February 2022

Nomenclature

W	Aerodynamic work per oscillation cycle [N.m]
X	Chord-wise coordinate
y+	Dimensionless wall distance
Φp	Phase of unsteady pressure coefficient (N^{th} harmonic) [deg]
σ	Inter blade phase angle [deg]
Ξ	Aerodynamic damping
CFD	Computational Fluid Dynamics
FFT	Fast Fourier Transform
FT	Fourier Transformation Method
IBPA	Inter Blade Phase Angle
PS	Phase-Shifted boundary condition
RANS	Reynolds Averaged Naiver–Stokes
A_i	Area elements projected into bending direction related to chord
A_N , B_N	Fourier coefficients for the Nth harmonic
$\vec{e}_n$	Normal unit surface vector pointing outwards
c_p	Amplitude of unsteady pressure coefficient
f	Frequency of blade vibration HZ
h (r)	Dimensionless bending amplitude to chord
$\hat{p}$	amplitude of the unsteady pressure
k	$k = 2 \bullet \pi \bullet f \bullet c / 2 \bullet v$ - reduced frequency
M_{is}	Isentropic Mach number
d_n	Nodal diameter
N_{bl}	Number of the rotor blades
N_h	Number of harmonics
N_s	Number of the stator blades
Nt	Number of time steps per oscillation cycle
$(\bar{\bullet})$	Time-averaged value
$(\tilde{\bullet})$	Unsteady perturbation value
$\vec{C}_{bl}$	Blade velocity vector [m/s]
T	Period of the vibrational cycle
p	Unsteady pressure
c	Length of the chord [m]
A_{mode}	Area of the blade in the bending mode [m^2]
L	Lower pitch-wise periodic boundary
U	Upper pitch-wise periodic boundary
$P_{tot,ref}$	Total pressure
$P_{sta,ref}$	Static pressure
$\phi_{p \to B}$	phase of the unsteady pressure in respect to the blade displacement

The mode shape of the blade is an important factor in determining the stability of the system (Bendiksen and Friedmann [4] and Firsching [5]). Their findings demonstrate the effect of bending-torsion coupling on the flutter boundaries. Also, computationally efficient models to predict the flutter based on the unsteady supersonic aerodynamic theory for cascades, have been developed and used to treat the coupled bending-torsion problem. Although they have proposed an efficient model, the extension of this analysis to a more sophisticated structural model needs to be investigated to evaluate the assumptions and models used in this study.

A stability parameter based on the influence coefficients of only the reference blade and its two closest neighbours, and the sensitivity of design parameters on blade stability was presented by Panovsky et al [6]. Furthermore, the methodology for utilizing the stability parameter in conjunction with a superposition of fundamental bending and torsion modes has been presented. The results show that the location of the torsion axis and the reduced frequency and, to a lesser extent, the steady blade loading, are of secondary importance [6].

To provide an efficient unsteady aerodynamic analysis, a three-dimensional, linearized Euler analysis to predict the aeroelastic and aeroacoustic responses of axial-flow turbomachinery blading was developed by Montgomery and Verdon [7]. They implemented numerical models into a computer code, called LINFLUX. As case studies, a helical fan and a three-dimensional version of the 10th Standard Cascade have been studied and the numerical results indicate that the developed three-dimensional aeroelastic and aeroacoustic analysis tool is reliable and effective [7]. The results indicate that the LINFLUX can provide accurate unsteady aerodynamic response information for these benchmark test cases, but for a better understanding of mesh requirements, enhancing the computational efficiency, and extending of its range of application, additional work is still needed [7]. Several numerical simulations have been

performed for different types of turbomachines to model these phenomena such as Poli et al[8] who offered a three-dimensional uncoupled and time-linearized approach for turbomachinery blade flutter analysis.

In another study, Rządkowski et al [9] carried out numerical simulations of 3D viscous flutter for bending oscillations of the 11th Standard Configuration by solving the 3D Reynolds-averaged Navier-Stokes equation, together with the Baldwin-Lomax turbulence model. Their developed numerical model uses the explicit monotonous second-order accurate Godunov-Kolgan finite-volume scheme and a moving hybrid H-O structured grid. The results showed sufficient quantitative and qualitative agreement of calculation and experimental studies for unsteady pressure amplitude, but there were some discrepancies for the phase distribution. Also, their method has shown some promise in the prediction of the aerodamping, but it is far from fully validated [9]. Some of these studies tried to find the major factors causing systems to be flutter prone. Clarck et al. [10] presented a time-linearized Navier–Stokes computational analysis of stall flutter in cascades. Their method was efficient and reliable in low speed and incidence conditions. In these conditions, increasing the reduced frequency, which is a dimensionless number that defines degree of unsteadiness, generally increases the aerodynamic damping. However, at high incidence, the aerodynamic damping of the least stable inter-blade phase angle decreases with increasing reduced frequency. They therefore stated that for understanding this phenomenon clearly, additional numerical and experimental studies need to be carried out.

Hansen [11] studied classical flutter for pitch-regulated turbines. It has been shown that flutter may occur on a pitch-regulated turbine, in blade tip overspeed and in large yaw misalignment. Reducing torsional blade stiffness and moving blade centre of gravity sufficiently aft of the blade cross sections also leads to higher flutter occurrences. However, due to the lack of experimental data for modern commercial turbines and computational limits, the effect of large flapwise blade deflection and the unsteady aerodynamic effects from the near wake of trailing vorticity on the predicted flutter have not been studied comprehensively. Ganiev et al [12] considered the flutter analysis of axial turbocharger turbine blades and found that the amplitude of oscillation can be raised by increasing the secondary damping of the acoustic length of the diagonal mode.

Nowadays, in new blade design, higher efficiency is demanded, and hence the blade loading increases, but to reduce the weight, the number of blades in any row and the blade thickness are decreased. The gap between rotor and stator is also reduced, which increases the flow interaction effects on the rotor blade. Furthermore, for cost considerations in turbochargers, blades are constructed integrated with the hub, rather than as bladed disks such as those used in larger turbomachinery. Therefore, there is no friction damping between the blades and the hub through a fir-tree connection, and hence dynamic stability analysis of blades is more critical [13].

Applying a nonlinear time marching method in flutter analysis for capturing multiple perturbations is computationally expensive, especially if the computational domain consists of whole stage. Therefore, most of the studies have only considered the rotor blades with time linearized methods. In this study, the nonlinear aerodynamic effects and deformations due to the centrifugal forces on the aeroelastic stability of a turbocharger turbine blade under real pulsating inlet conditions are investigated using a time marching solution. The effect of the blade thickness distribution on the stability of the system is discussed which has not been studied in the previous literature for radial turbocharger turbines. For this purpose, the whole domain is simulated to take into consideration the flow incidence angle and the effect of disturbance forces due to the interaction of rotor and stator.

2. Flutter analysis method

The differential equations of motion of the aeroelastic system can be written as:

$$[\mathrm{M}]\left\{\ddot{\mathrm{X}}\right\}+[\mathrm{G}]\left\{\dot{\mathrm{X}}\right\}+[\mathrm{K}]\{\mathrm{X}\}=\{\mathrm{F_{ae}(t)}\} \tag{1}$$

where [M], [G] and [K] represent modal mass, modal damping and modal stiffness matrices, respectively.$\{X\}$ is the modal coordinate vector and $\{F_{ae}(t)\}$ is the modal unsteady aerodynamic force vector that includes the upstream and downstream aerodynamic disturbances of the blade as follows [14]

$$[\mathrm{M}]\left\{\ddot{\mathrm{X}}\right\}+[\mathrm{G}]\left\{\dot{\mathrm{X}}\right\}+[\mathrm{K}]\{\mathrm{X}\}=\left\{\mathrm{F_{disturbance}(t)}+\mathrm{F_{damping}(t)}\right\} \tag{2}$$

Aerodynamic damping can be determined from the solution of Eq. (2) which can then be used to investigate the aeroelastic stability of the system. The coupling of the structural part of Eq. (2) with unsteady aerodynamic forces due to blade motion was treated in a time marching solution. Mass and momentum equations of the flow around the vibrating blades are solved using CFD numerical methods. The kinematic relationship between individual and travelling blade wave motion (X and X_{σ_n}) with the inter-blade phase angle σ_n is given as [15]:

$$\mathrm{X}=\mathrm{EX}_{\sigma_n}\mathrm{e}^{\mathrm{j}\omega t} n=0,\cdots,N-1 \tag{3}$$

$$E_{i,n}=e^{j\frac{2\pi in}{N}} n=0,\cdots,N-1 \tag{4}$$

When the blades vibrate at the same mode shape, frequency, amplitude and inter-blade phase angle (IBPA), this refers to the travelling wave mode (TWM) condition. The IBPA is the phase lag between the blades when they reach their maximum amplitude [14] and it is a function of the number of blades (N_{bl}) and nodal diameter (d_n) as

$$\sigma_n=\frac{2\pi\bullet d_n}{N_{bl}} \tag{5}$$

It is noted that the nodal diameters are lines of zero displacement during the vibration of the disk [14]. The number of nodal diameters is the number of wavelengths that fit in the whole annulus and for the n[th] harmonic excitation can be presented as [16].

$$d_n = \left| nN_s - N_{bl} \left\lfloor \frac{nN_s + \left\lfloor \frac{N_{bl}}{2} \right\rfloor}{N_{bl}} \right\rfloor \right| \tag{6}$$

where, N_{bl} is the number of rotor blades, N_s is the number of stator blades and n is the number of harmonics. The floor function in Eq. (6) leads to having an integer number of nodal diameter. In this study, the number of rotor and stator blades of the turbine are $N_{bl} = 12$ and $N_s = 24$, respectively. For the first and second harmonics, the nodal diameters can be obtained as:

$$d_1 = \left| 24 - 12 \times \left\lfloor \frac{24+6}{12} \right\rfloor \right| = 0 \tag{7}$$

$$d_2 = \left| 48 - 12 \times \left\lfloor \frac{48+6}{12} \right\rfloor \right| = 0 \tag{8}$$

Both diameters are zero, which means that all blades vibrate in the same phase and all blades are aligned.

2.1. The Fourier Transformation method

The Fourier Transformation (FT) method is used for reducing the number of passages required to be analysed to two. In this method, a phase-shifted periodic boundary condition is used and the flow specifications at the pitch-wise intersections of neighbour passages are periodic in time; so, Fourier series could be applied for storing the results at boundaries (Eq. (9)). A remarkable decrease in the required storage volume was caused by the method proposed by He [17] in comparison with the previous approach which stored the whole time-periodic results during each vibration cycle [18].

$$\widehat{f}(t) = \sum_{m=-M}^{m=M} A_m e^{-j(\omega m t)} \tag{9}$$

Wakes due to the rotor–stator interaction were treated applying Eq. (9) which transfers flow properties between interfaces with different widths. It is based on this assumption that the relative position of the stationary and rotating regions is periodic in time steps [19]. Fourier coefficients are collected at the intersection layer of two adjacent passages. For rotor–stator interfaces, double time and azimuthal Fourier series decomposition, as presented in Eq. (10), can be used [20].

$$\widehat{f}(t,\theta) = \sum_{n=-N}^{N} \sum_{m=-M}^{m=M} A_{n,m} e^{-j(\omega m t + n\theta)} \tag{10}$$

Flow parameters for upper and lower boundaries are defined as Eqs. (11) and (12).

$$U^u = \overline{U} + \sum_{N=1}^{N_h} [A_N.Sin(N\omega t + \sigma) + B_N.Cos(N\omega t + \sigma)] \tag{11}$$

$$U^l = \overline{U} + \sum_{N=1}^{N_h} [A_N.Sin(N\omega t - \sigma) + B_N.Cos(N\omega t - \sigma)] \tag{12}$$

$$\overline{U} = \frac{\omega}{2\pi} \sum_{t=1}^{N_t} U.\Delta t \tag{13}$$

Phase shifted boundaries can be considered as normal periodic boundaries after three vibrational cycles. $\boldsymbol{A_N}$ and $\boldsymbol{B_N}$ are Fourier coefficients which are calculated in time steps during vibrational cycles as

$$\boldsymbol{A_N} = \frac{\boldsymbol{\omega}}{\boldsymbol{\pi}} \sum_{t=1}^{N_t} \boldsymbol{U.Sin(N\omega t)} \bullet \boldsymbol{\Delta t} \tag{14}$$

$$\boldsymbol{B_N} = \frac{\boldsymbol{\omega}}{\boldsymbol{\pi}} \sum_{t=1}^{N_t} \boldsymbol{U.Cos(N\omega t)} \bullet \boldsymbol{\Delta t} \tag{15}$$

2.2. Domain definition

The domain consists of a 30° volute sector, two stator blade passages, two rotor blade passages and a 60° diffuser sector. The circumferential boundaries of the stator and rotor domains are periodic interfaces. Fig. 1 shows the volute and the replaced sector. For

modelling the whole volute with a 30-degree sector and normal inlet flow, Japiske and Baines's [21] method is incorporated. The flow with free vortex assumption (Eq. (16)) is solved by introducing a swirl coefficient (S in Eq. (17)) of 0.9 for compensating the neglected tangential momentum at the inlet.

$$r_1, C_{\theta 1} = r_2, C_{\theta 2} \tag{16}$$

$$r_1, C_{\theta 1} = Sr_2, C_{\theta 2} \tag{17}$$

By substituting the assumption of incompressible flow (Eq. (18)) into Eq. (16), the radial velocity component is obtained from the tangential velocity component as presented in Eq. (20)

$$\rho u_1, A_1 = \rho C_{r2}, A_2 \tag{18}$$

$$\rho C_{\theta 1}, A_1 = \rho C_{r2}, A_2 \tag{19}$$

$$\frac{Sr_2}{r_1} \bullet \frac{A_1}{A_2} C_{\theta 2} = C_{r2} \tag{20}$$

2.3. Boundary condition

To study the effect of unsteady, pulsed flow on the aeroelastic instability, the diagram of the simulated pulse flow (using a set of rotating chopper plates to create gas pulses) for 50% speed is used for definition of the volute inlet pressure [22] which is shown in Fig. 2 in which chopper angle coincides with the crankshaft angle.

During an input pressure pulse across 360 degrees of chopper angle the rotor wheel completes 11 revolutions at 53344 rpm. The outlet static pressure profile is also defined as the outlet boundary condition. The total inlet temperature is assumed constant and equal to 300 K. It is important to note that simulations are carried out under transonic flow conditions. The computational domain for unsteady simulation is depicted in Fig. 3 and the computational domain for steady analysis is shown in Fig. 4. The length of the diffuser is considered much longer than the characteristic length of the rotor to prevent the flow return.

2.4. Mesh

High-quality meshing was applied in Turbogrid with automated and mesh optimized topology (ATM) which makes the O-grid for boundaries layers and hexahedral meshes for other parts. At least ten nodes have been used for resolving the boundary layer. Boundary layer expansion ratio was set as 1.2. The height of the first cell is obtained from Eq. (21) as follows

$$\Delta y = Ly^+ \sqrt{80} Re^{\frac{-13}{14}} \tag{21}$$

where L is the characteristic length of the rotor or the length of chord, which is considered to be $L = 60$ mm. The Reynolds number for the ideal gas density with the dynamic viscosity of 2×10^5, and the relative gas velocity of 200 m/s, is about 6×10^5, therefore by using Eq. (21), the height of the first mesh can be obtained as 0.002 mm. Fig. 5 shows the mesh density study of the steady state part of the simulation, which is obtained by comparing the circumferentially averaged total pressure loss coefficient at the end of the rotor through five trials.

As shown in Fig. 4, by increasing the mesh density from trial 1 to trial 5, the pressure loss coefficient shows less variability and gets more accurate. Trial 5 has a finer mesh than trial 4, but the pressure loss coefficient values are equal therefore, to save the computational cost of the analysis, the mesh size of trial 4 is selected. The results in unsteady state become more reliable by making the mesh finer. Table 1 summarizes the number of elements in each member in unsteady state simulation.

Fig. 6 shows the stator and rotor blade meshing in unsteady state simulation. The mesh displacement is considered using the mesh

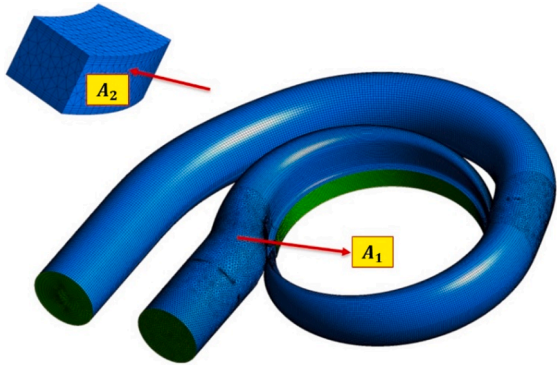

Fig. 1. Volute sector selection for unsteady analysis.

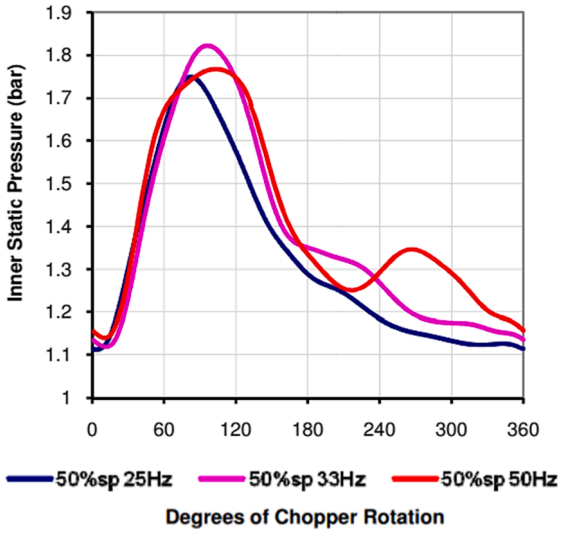

Fig. 2. Inlet static pressure [2].

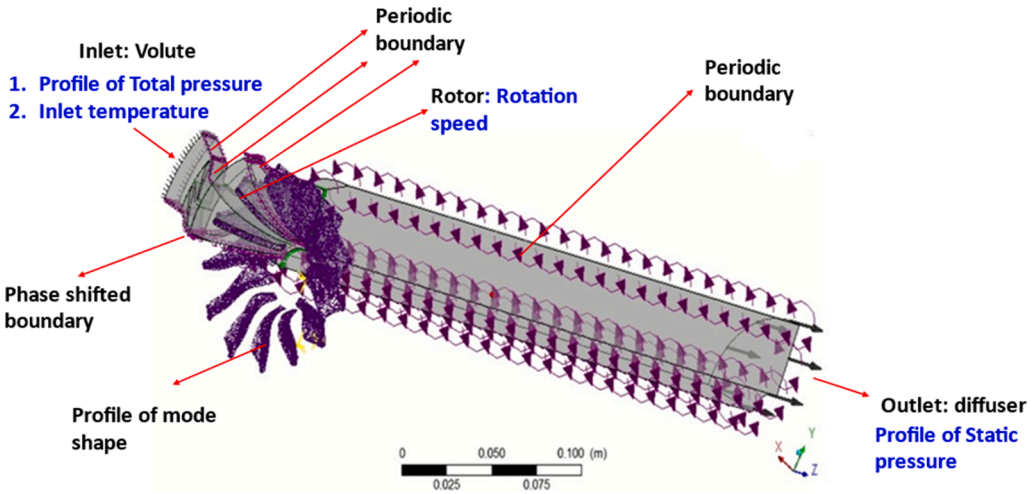

Fig. 3. Computational domain (Unsteady simulation).

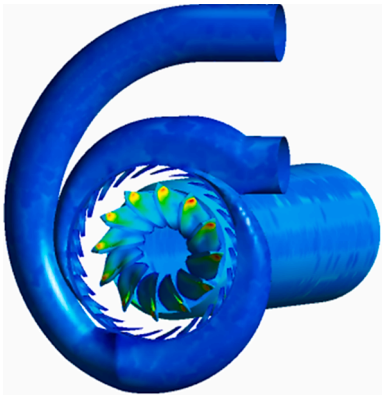

Fig. 4. Computational domain (steady state simulation).

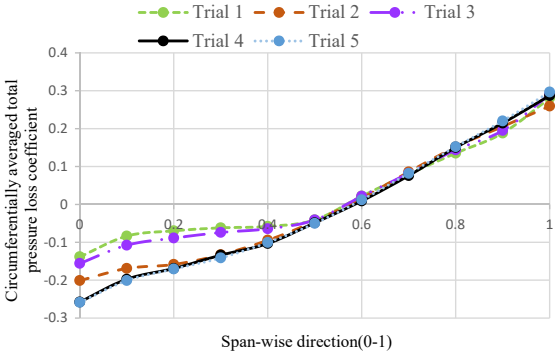

Fig. 5. Circumferentially averaged total pressure loss coefficient at the end of rotor.

morphing method. Mesh stiffness is considered variable through an expression, which is inversely proportional to the volume of the finite volume elements in order to preserve the mesh quality and to reduce the mesh deformation.

The mesh displacement factor is considered to be equal to 0.001, which means that the maximum displacement of the blade tends to be about 1% of the chord length in the mid-span. Therefore, the selected mesh is able to capture the pressure fluctuations without significant deformations. The displacement diffusion equation (Eq. (22)) is applied to diffuse the displacement of the blade wall boundaries to the surrounding nodes as well as maintaining the relative position of the initial mesh.

$$\nabla.\left[\Gamma_{\text{disp}}\nabla\delta\right] = 0 \tag{22}$$

where δ is the mesh displacement and Γ is the mesh stiffness. This equation is solved for each time step of unsteady simulation and for each iteration in steady simulation. Variable mesh stiffness sustains the quality of the meshes after displacement. Mesh stiffness is calculated by Eq. (23):

$$MeshStiffness = 1\bullet\left[\frac{\text{m}^2}{\text{s}}\right] \times \left(\frac{1.0\text{E}-6[\text{m}^3]}{\text{VolumeofFiniteVolumes}}\right)^2 \tag{23}$$

As the mesh stiffness is a function of the control volume size, in smaller volumes the mesh is stiffer with lower deformation.

2.5. Numerical method

The vibrating blade row is simulated using CFX17 in a travelling wave mode by applying a Fourier Transformation (FT). The flow separation effects, captured using the viscous Reynolds-averaged Navier-Stokes (RANS) equations with SST-kω turbulence model and curvature correction, are solved in a time-marching manner. The high-resolution advection scheme is used for equation discretizing. The initial condition for the transient solver is obtained by the steady state simulations. It is noted that the pressure based, implicit, coupled solver for mass and momentum equations uses an algebraic multi-grid method. Computations are performed with double precision. Table 2 presents the unsteady state simulation setup. The periodic behaviour of the fluid properties in transient simulation, with less than 0.01% variation, is obtained in 65 days with a supercomputer system with two 3.8 GHz Zenon 8-core processors and a total of 16 cores. The system had a processing speed of about 62 GHz and processing power of 550 Gigaflops.

Performance parameters of turbine in steady state simulation and measurement were compared for validation purpose. Fig. 7 compares the mass flow rate versus pressure ratio from measurement [22] and the simulation. It is clear that the results are in good agreement with measurement.

Fig. 8 compares the results of the unsteady simulation with the experimental data [22]. The obtained results follow the trend of the measured data.

In Fig. 8 at the beginning of the simulation, the measured results vary from the simulation by about 10% which is due to the completion of the Fourier coefficients, and at the second revolution, the variability of the results is about 4%, which is acceptable for subsequent calculations.

Table 1
The number of elements in each member (Trial 4).

	Volute	Stator	Rotor	Diffuser
Element type	Unstructured Prism Tetrahedral	Structured Hexahedral	Structured Hexahedral	Unstructured Tetrahedral
Numbers	212,455	2,215,268	3,817,836	535,880

(a) (b)

Fig. 6. a) stator blade meshing **b)** Rotor blade meshing.

Table 2
The unsteady state Simulation setup parameters.

Time steps	1.29939e−06
Vibration cycle duration	0.000203 Sec
Number of time steps in one cycle	156
Whole modelled time steps	1351
Number of rotor revolution in performed simulation	1.42
Rotor speed	53344 rpm
Number of vibration cycles	9
Simulation Duration	65 days

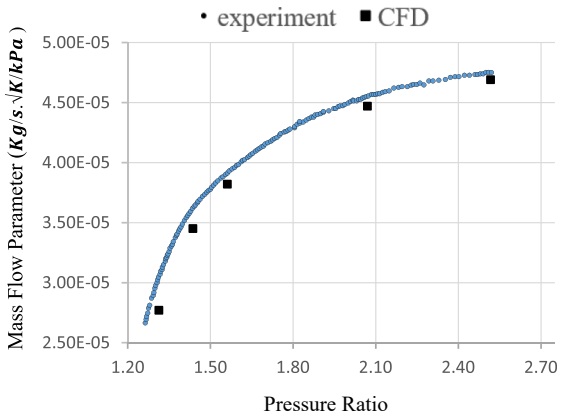

Fig. 7. Comparison of computed and measured mass flow parameter against pressure ratio.

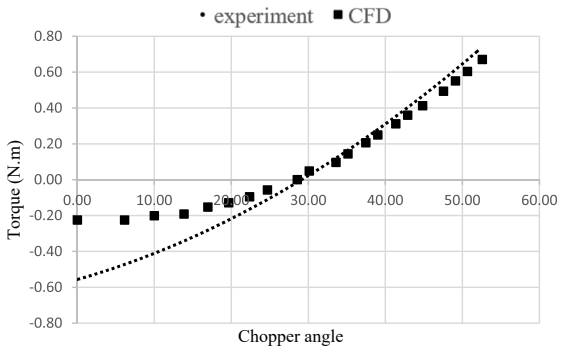

Fig. 8. Torque measurement results under in-phase pulsations (50 %sp 50 Hz) and turbine simulation.

2.6. Mode shapes

To interpolate the positions of nodes at the blade boundary during each time step, blade positions at zero and max displacements of oscillation in selected mode shapes should be obtained. The mode shapes and natural frequencies of the rotating rotor blade are determined by eigenvalue extraction using Ansys APDL. The blade is made of nickel superalloy 713. The first flexure and the first torsion mode shapes of the blade are shown in Fig. 9. It is noted that the first mode shape is the first flap-wise bending with the frequency of 4935 Hz, and the second mode is the first torsional mode with a frequency of 12841 Hz at a rotor speed of 889.066 Hz.

2.7. Campbell diagram

For flutter analysis, the frequency of the flutter is assumed to be known data, and hence a Campbell diagram is used to find the modal behaviour of the system in the time domain approach of solving aero elastic models. Forced resonance points and possible propagating stall or flutter excitation could happen at the coincident points of natural frequency, rotor rotational speed and excitation (engine) order. In turbomachines, the failures are generally linked to either the first flexure or the first torsional mode without coupling, due to the high mass ratio between the blades and the hub [3]. Therefore, in this study the excitation of first harmonic in the design speed was investigated. From the Campbell diagram in Fig. 10, the frequency of the red point was assumed as the flutter occurrence frequency as it is the point of coincidence of the first bending mode line with the 6th excitation order line and rotor speed.

The excitation order (EO) indicates the number of excitations of the rotor blade per rotor rotation, and slope of the EO lines is equal to the Vane Passing Frequency (VPF), which is defined as [23].

$$\mathrm{VPF} = \omega \times N_s \tag{24}$$

where ω is the frequency of a pressure oscillation cycle and is equal to the time required for the blade to travel the distance between two stator blades. Therefore, the first harmonic pressure in EO of 24, results in a VPF of 21337.6 Hz. When the rotor rotates at a design speed of 53344 rpm (889.066 Hz), the first natural frequency crosses the harmonic frequency in excitation order (EO) of 6.

2.8. Aerodynamic damping

Aerodynamic damping is caused by the unstable pressure field in the fluid due to the vibration of the blades. Flow velocity, mode shape, frequency and nodal diameter can affect this type of damping. Aerodynamic damping is the criterion for detecting the occurrence of flutter [3], because aerodynamic damping could have a negative value. In this situation the fluid increases the blade's vibration amplitude and if sufficient mechanical damping was not available, blade failure would occur. There is no friction damping in the integrated discs, and the only source of mechanical damping is damping within the material [16].

In this study, two methods are used to find the aerodynamic damping. In the first approach, the damping is calculated by using the phase of the unsteady pressure coefficient and the area element. In the second approach (energy method), the damping can be determined by integrating the aerodynamic work during one oscillation cycle. To calculate the pressure coefficient in the first approach and at point x, the following equations can be used in which $P_{dyn,ref}$ is the dynamic pressure [24].

$$\mathbf{C_p}(\mathbf{x}) = \frac{\mathbf{P}(\mathbf{x})}{\mathbf{P_{dyn,ref}}} \tag{25}$$

$$\mathbf{P_{dyn,ref}} = \mathbf{P_{tot,ref}} - \mathbf{P_{sta,ref}} \tag{26}$$

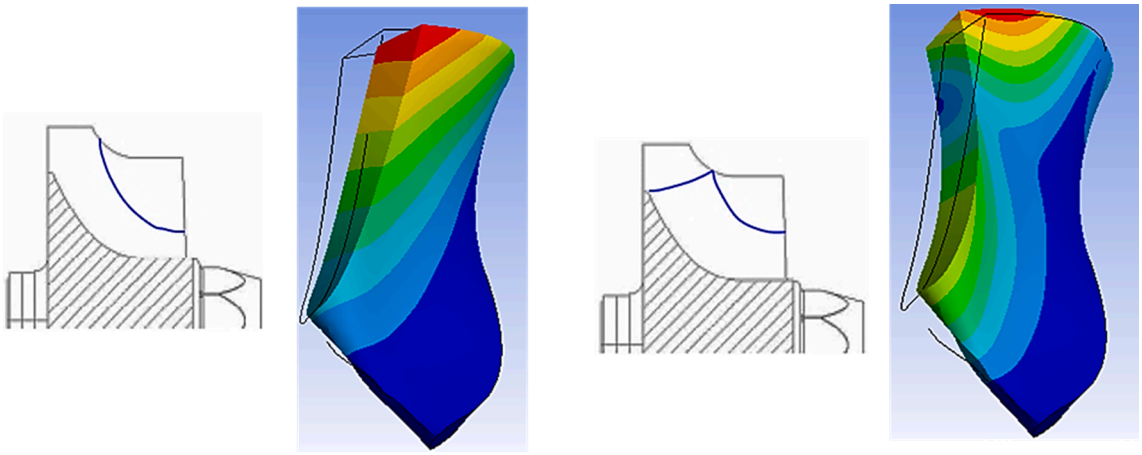

Fig. 9. Structural dynamic characteristics of blade a) first flexure b) first torsional.

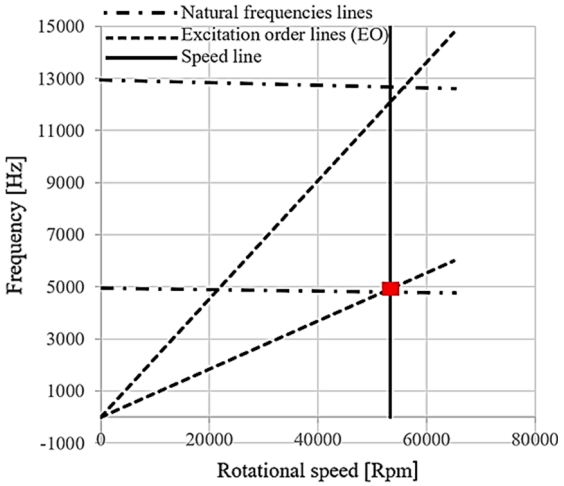

Fig. 10. Campbell diagram from modal analysis.

The unsteady oscillation of the blade can be defined as

$$\beta(t) = R\{\beta \mathbf{e}^{\mathbf{i}(\omega \mathbf{t})}\} \tag{27}$$

where β is the blade vibration amplitude in degrees. The pressure at desired point x will be obtained by Eq. (28) as follows:

$$\mathbf{P}(x,t) = P(x) + \mathbf{R}\left\{\mathbf{P}(\mathbf{x},\mathbf{t})\right\} = \mathbf{P}(\mathbf{x}) + \mathbf{R}\left\{\widehat{\mathbf{P}}(\mathbf{x})\mathbf{e}^{\mathbf{i}\left(\omega \mathbf{t}+\varphi_{\mathbf{p}\to\mathbf{B}}\right)}\right\} \tag{28}$$

where R is the real part and $\varphi_{p\to B}$ is the phase angle between the unsteady force and blade motion. Finally, the unsteady pressure coefficient can be defined as

$$\mathbf{C_p}(\mathbf{x},\mathbf{t}) = \frac{\mathbf{R}\left\{\mathbf{P}(\mathbf{x},\mathbf{t})\right\}}{\beta \mathbf{P_{dyn,ref}}} = \frac{\mathbf{R}\left\{\widehat{\mathbf{P}}(\mathbf{x})\mathbf{e}^{\mathbf{i}\left(\omega \mathbf{t}+\varphi_{\mathbf{p}\to\mathbf{B}}\right)}\right\}}{\beta \mathbf{P_{dyn,ref}}} = \frac{\mathbf{P}(\mathbf{x},\mathbf{t})}{\mathbf{h}(\mathbf{r})\left(\mathbf{P_{tot,ref}} - \mathbf{P_{sta,ref}}\right)} \tag{29}$$

The first harmonic is calculated from the Fast Fourier Transformation (FFT) on the unsteady pressure coefficient. The amplitude of pressure coefficient, $C_{p,amp}$, can be determined using the following equation:

$$\mathbf{C_{p,amp}}(\mathbf{x}) = \frac{\mathbf{R}\{\widehat{\mathbf{P}}(\mathbf{x},\mathbf{t})}{\beta \mathbf{P_{dyn,ref}}} \tag{30}$$

$\mathrm{C_{p,phase}}(\mathrm{x})$ is phase of unsteady pressure coefficient in desired point which is defined as:

$$\mathrm{C_{p,phase}}(\mathrm{x}) = \phi_{p(x)} - \phi_{\beta} \tag{31}$$

The aerodynamic damping is obtained by Eq. (32).

$$\Xi = -\int_{A_1} \widetilde{C}_{p,(1)} \cdot sin\left(\phi_{p,(1)}\right) dA_i \tag{32}$$

where A_i is the area elements, which are negative on the suction surface and positive on the pressure surface. The regions with negative aerodynamic damping are known as aerodynamically unstable regions. In the energy method, aerodynamic work is calculated by numerically integrating the surface unsteady pressure over the whole blade surface in one cycle of vibration as shown in Eq. (33).

$$W = \int_T^{t=T} \left[\int_a \frac{\left(\widetilde{P} \cdot \left(\overrightarrow{C}_{bl} \cdot \overrightarrow{e}_n\right)\right)}{h(r)^2} \cdot dA \right] \cdot dt \tag{33}$$

where p is the unsteady pressure amplitude, h is dimensionless bending amplitude, $\overrightarrow{e}_n$ is the surface normal unit vector and $\overrightarrow{C}_{bl}$ is the blade velocity vector in respect to the blade displacement. Fourier coefficients are calculated in every vibration cycle and are updated once a period.

Aerodynamic damping of each blade is calculated using aerodynamic work as equation (34) [16]:

$$\Xi = \frac{-W}{\pi . c . A_{mode} . \left(\overline{P}_{t,1} - \overline{P}_1\right)} \tag{34}$$

3. Results

From the energy method and Eq. (34) aerodynamic damping for the last period is obtained equal to a negative value of −0.000325 for an inter blade phase angle of zero. The negative aerodynamic damping indicates that flutter occurrence is probable, in that case the cascade oscillation isn't damped, and the fluid adds energy to the blade during oscillation causing an increase in vibration amplitude until blade failure occurs. The first harmonic is calculated from the Fast Fourier Transformation (FFT) on the unsteady pressure coefficient. The result of the simulation is shown in Fig. 11 and is compared with the experimental and simulation results by Drek et al [24]. The amplitude of the unsteady pressure coefficient for the last time step is shown in Fig. 11-a, and the phase of the unsteady pressure coefficient is shown at 0.5 span in Fig. 11-b.

Flutter is prone to occur when the aerodynamic damping changes sign from positive(stable) to negative(unstable). A region of instability is recognized in Fig. 11-b after mid-span on the suction side, but the pressure surface shows no aerostatic instability.

A comparison of aerodynamic damping in variable inlet pressure is shown in Fig. 12. 53 degrees of chopper angle have been modelled with ascending pressure trend (Fig. 2).

Fig. 12-a shows aerodynamic damping calculated by full period integration versus accumulated time steps. Inlet pressure (Fig. 2) is not constant in all time steps so aerodynamic damping is changing in accordance with variable inlet pressure. In lower pressures, the blade is more stable. Fig. 12-b shows the aerodynamic damping in accumulated timesteps. The first 1400 steps r relate back to steady state simulation for finding the initial condition, also 600 timesteps (timesteps (25 degree of chopper angle) are taken to allow the Fourier coefficient to follow the physics (Fig. 8) so the aerodynamic damping was pictured in the figure from the 2000th timestep. By increasing the inlet pressure, the aerodynamic damping sign changed from positive in 2300th timesteps to negative. The translation to negative values happened at an inlet pressure of 1.8. In Fig. 12-b aerodynamic damping fluctuation damped by time so the flutter would be stable.

Fig. 13 shows the aerodynamic work distribution on the blade surface for zero IBPA in one vibrating cycle. From Fig. 13 it can be seen the suction surface shows an area of positive work distributed from 0.3 to 0.9 chord-wise, whereas the pressure surface shows sporadic small regions of positive work on the blade. The blade is flutter prone in the areas of positive work.

The steady state analysis was performed using a 3D NS solver using ANSYS CFX. Mach number distribution at 0.3, 0.5, and 0.9 spans are shown in Fig. 14. In this figure separation point, transition point and reattachment point are shown with S, T and R respectively.

On the pressure side in Fig. 14, results show a strong leading edge drop and subsequent shock. The shock position defines the transition regions of stabilizing/destabilizing. It can be seen that relative Mach number distribution at 0.3 blade span has higher values compared to other heights, and shock happens at 0.4 chord on pressure-side which leads to produce positive work.

In Fig. 11-b and 14 the flutter instability happens after a supersonic region. From Figs. 13 and 14 it can be seen that positive work area is located after the separation bubble on the suction surface. In fact, the local excitation is very strong in the area near 60% chord on the suction side. Shock excites flutter prone area but only the continuous positive work regions make unstable region(at 0.6 span of the suction side).

Fig. 15 shows the vortices in turbine passages due to separation and flow leakage. Two unstable regions are exits in the blade passage, the Horseshoe vortex near to suction side at section A and the Tip Leakage vortex next to the shroud of the pressure side. The Horseshoe vortex is produced by the incidence of the inlet pressure and stagnation of the blade. This vortex only spans over the first quarter of the blade chord (in section A see Fig. 15-a-b-c). Considering work distribution in Fig. 13, it can be concluded that this vortex produces some positive work at 0.1 chord of the suction side.

Tip Leakage vortex is formed in section B (Fig. 17-c). This vortex makes an unstable region on the upper half of the suction side (Fig. 17-b). Evidence of positive work at 0.4 chord-wise on the pressure side in Fig. 13, shows that the Tip leakage vortex also contributes to positive work. In both the Tip Leakage vortex and Horseshoe vortex, the fluid is doing work on the blade and triggers the flutter instability.

Fig. 14 clearly indicates that at lower spans the blade excitation, due to oscillations, is substantially increased. This is confirmed by presence of the Horseshoe vortex near to pressure side at section A at Fig. 15-b and a Leakage vortex next to the shroud and suction side on section B at Fig. 15-c. The Leakage vortex excites the same area of the suction side which is unstable in Fig. 15-a (area after 0.4 chord on suction side). Also force contours in Fig. 15-d show the energy feeding area on the blade surface in the vicinity of the 0.2–0.4 span on the pressure surface. Although this makes an area of positive work, it does not lead to instability of that region.

To study the effect of flow dynamics on the flutter occurrences probability, the velocity contours at steady and unsteady analysis are shown in Fig. 16.

Velocity contours in the steady and unsteady analysis (Fig. 16-a and b) show similar flow behaviour. Therefore, the vortex features in the steady analysis can be analysed for aeroelastic stability. From this figure it can be seen that a positive work area is located after the separation bubble on the suction surface. In fact, the local excitation is very strong in the area near 60% chord on the suction side. On the pressure side, the shock oscillations are responsible for the positive work.

The effects of inlet pressure condition on blade stability are investigated. The steady state simulation was run with five different inlet pressure conditions. Table 3 shows the inlet pressure of each case. The results given in Fig. 17, clearly indicate from case c5 to c1, the separation bubbles get smaller, and flow attaches the blade sooner, therefore increasing the inlet pressure leads to higher

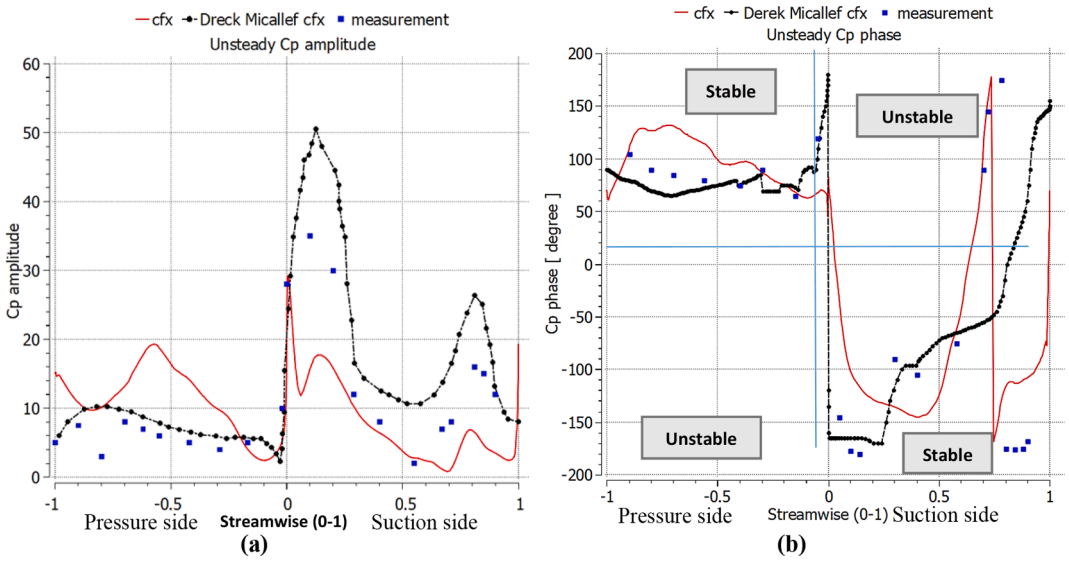

Fig. 11. a) Amplitude of the unsteady pressure coefficient [-] at 0.6 chord (1st harmonic) **b)** Phase of the unsteady pressure coefficient [degree]at 0.5 span (1st harmonic).

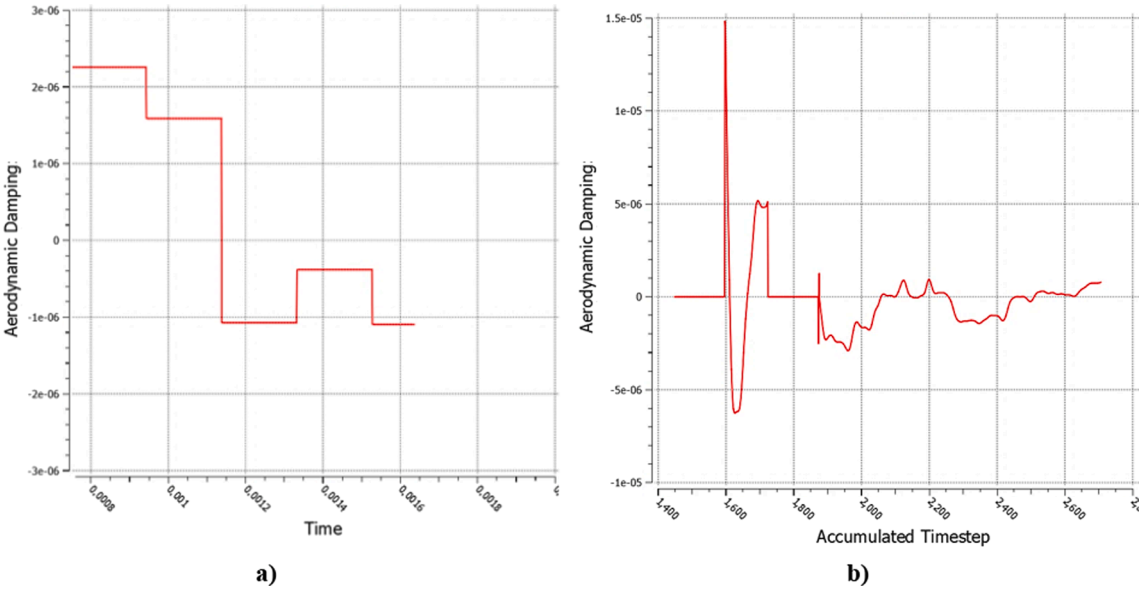

Fig. 12. a) Aerodynamic damping (full period integration) versus time **b)** Aerodynamic damping (moving integration interval) versus accumulated time steps.

instability.

In the next step, the effect of blade thickness distribution on the blade stability is investigated. The 3D CFD analysis is carried out for the rotor blade with different thickness of t_{max}, L_E and T_E radius to verify the Mach distribution on the blade surface. The results are shown in Fig. 18 and the blade profile characteristics are given in Table 4.

A relative Mach number higher than 1 was achieved on 0.1 chord of the pressure side for all blade designs as shown in Fig. 18. However, Profiles "a" and "e" by the highest T_E radius show a stronger expansion and shock intensity on the pressure side and on the suction side they show a smaller separation bubble in comparison with other profiles, as the reattachment point is located closer to the leading edge of the blade. This indicates that higher T_E radius leads to better stability. Comparing profiles "c", "b" with equal T_E and L_E radius but different t_{max}, proves that a profile with higher t_{max} has a leaner shock on the pressure side but similar Mach distribution on suction side, which results in similar stability. Also, profiles "c", and "d", in spite of having different L_E radius, show similar Mach number distribution. Comparing the Mach number distribution shows that the effect of T_E radius dominates, and profile with higher T_E

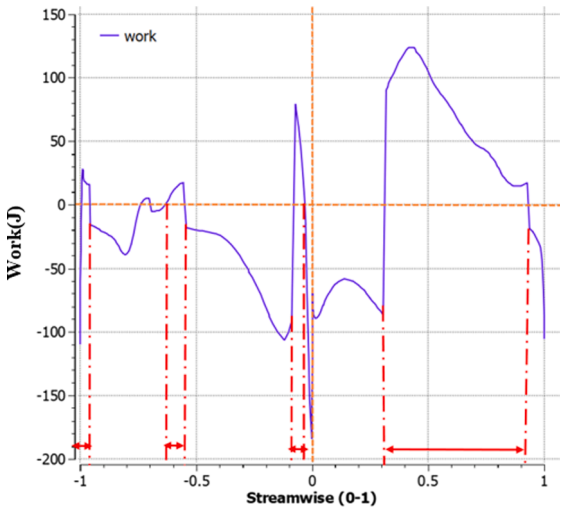

Fig. 13. Distribution of aerodynamic work on blade surface in one vibrating cycle from unsteady analysis.

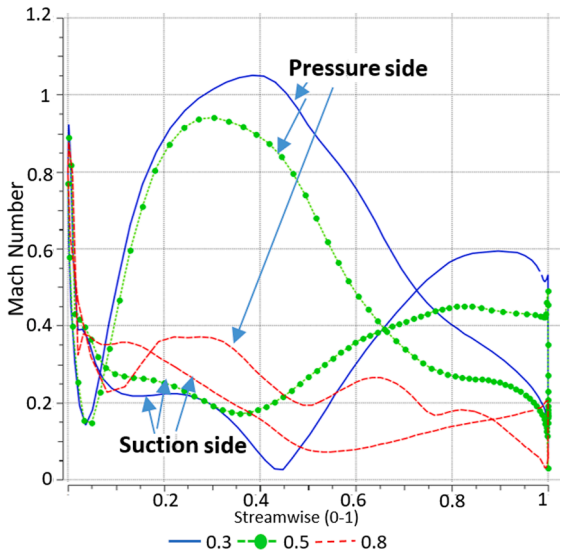

Fig. 14. Mach number in different heights from steady analysis.

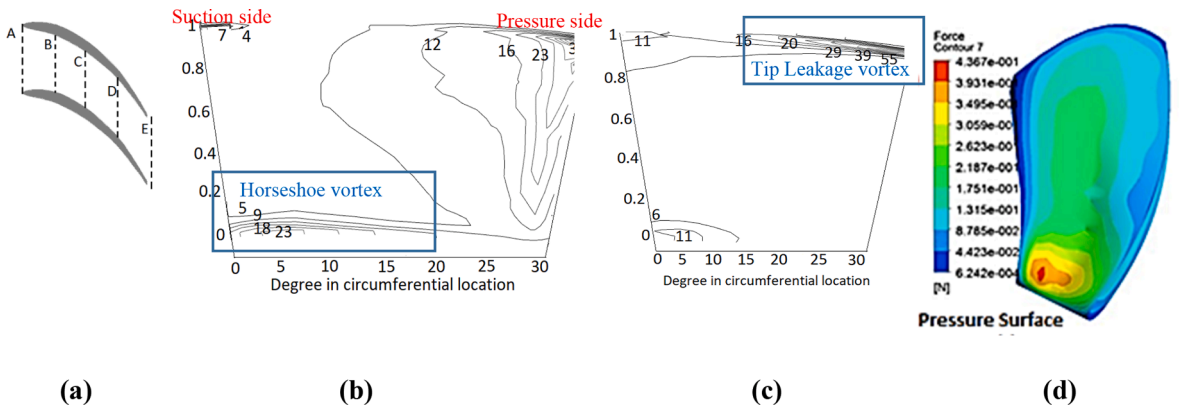

Fig. 15. **a)** Passage sections **b)** Vorticity contours at section A **c)** Vorticity contours at section B **d)** Force contours.

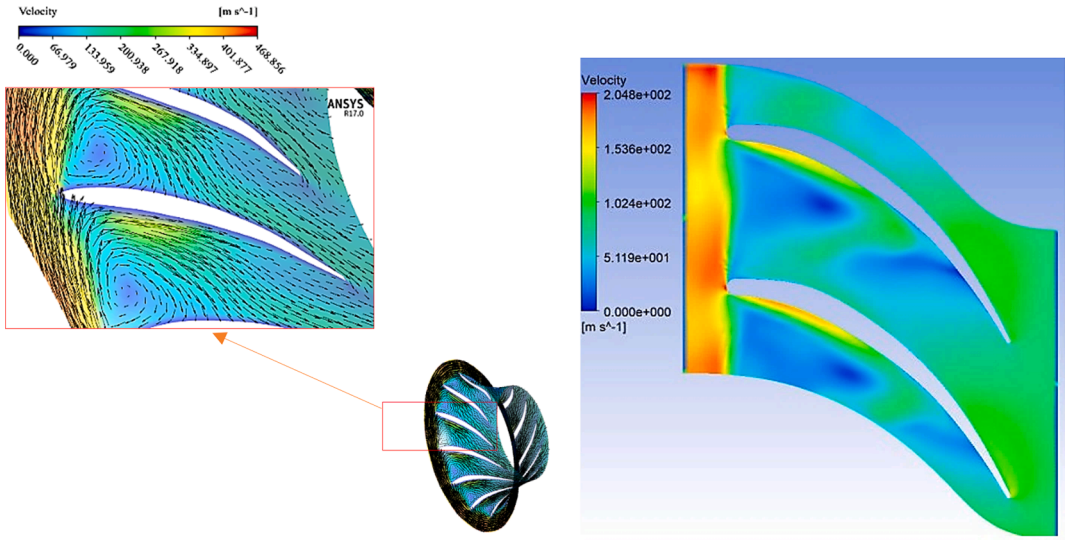

Fig. 16. a) Velocity contours at steady analysis **b)** Velocity contours at unsteady analysis.

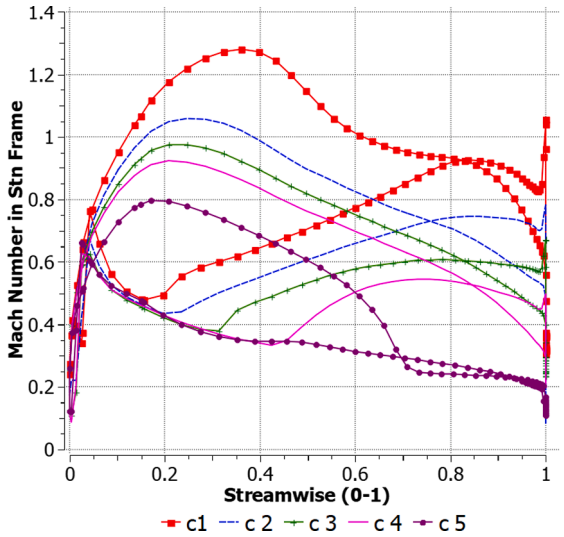

Fig. 17. Mach distribution in different inlet pressure conditions on 0.01 span steady analysis.

Table 3
Inlet boundary conditions.

	Case 1	Case 2	Case 3	Case 4	Case 5
Total Pressure [pa] At lower inlet	259,358	210,792	159,073	146,303	134,649

radius have better aeroelastic stability. The meridional variations of pressure on turbine blade for profiles “a”, “b” and “c” are shown in Fig. 19.

Fig. 19 shows that the advantage of using a thicker blade profile from midspan out to the tip. The pressure has decreased significantly by reducing the maximum thickness(tmax). Increasing trailing edge radius, results in higher load at the trailing edge region but better stability.

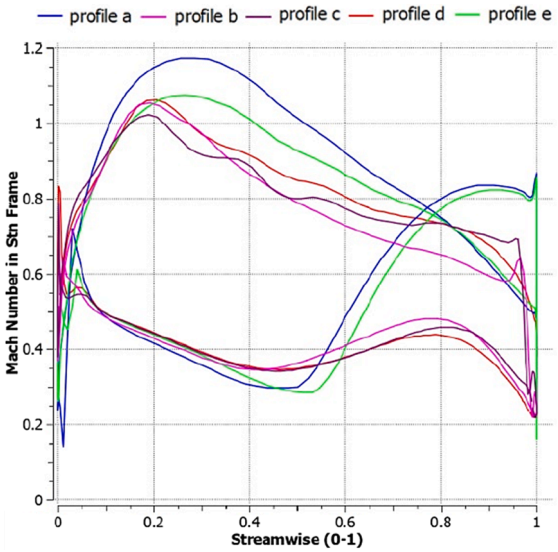

Fig. 18. Mach distribution on different blade profiles in equal admission on 0.01span.

Table 4
Blade profile characteristics.

	LE radius (mm)	*TEradius* (mm)	$t_{max}(mm)$	Efficiency %
Profile a	0.6	0.5	2.8	61.55
Profile b	0.8	0.375	2.8	59.71
Profile c	0.8	0.375	3.6	46.16
Profile d	0.6	0.4	2.75	63.34
Profile e	0.65	0.5	3	54.08

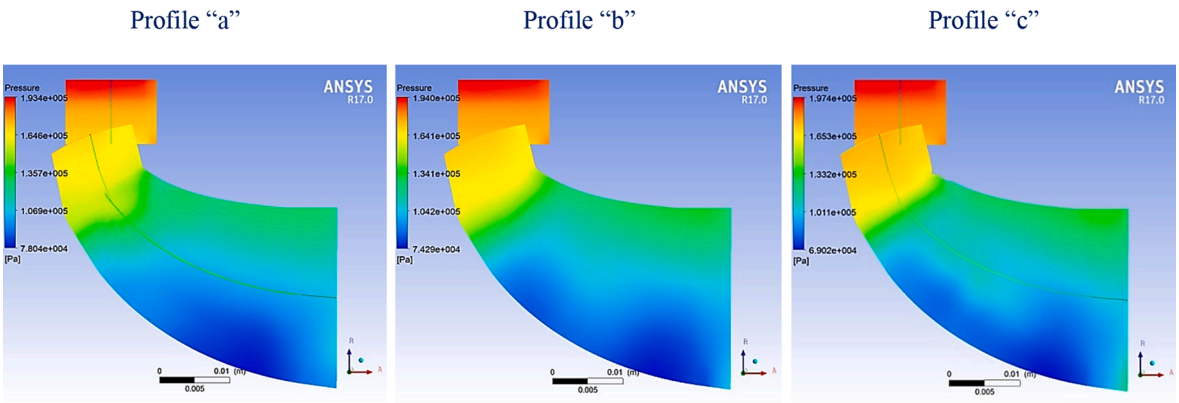

Fig. 19. Meridional variations of pressure on 3 turbine blade profiles.

4. Conclusion

The present study focuses on the flutter stability analysis of a pulsating loaded radial turbocharger turbine through 3D computational fluid dynamics simulations at the design point and IBPA of zero. Aerodynamic damping is calculated for the first flexure mode of vibration. The results show that vibrations are not damped in the first bending mode of this radial turbocharger turbine in transonic condition at design point but are amplified by the fluid, so a visible margin of probable flutter was noticed.

Results show that a strong leading-edge drop, and subsequent shock may happen before 0.1 span, about 0.6 span and at trailing edge. Shock excites the flutter prone area but only the continuous positive work regions contribute toward the flutter and make the unstable region at 0.6 span of suction side.

Taking into account the effects of inlet flow condition on stability margin, a series of steady 3D computational fluid dynamics

simulation has been carried out. The results showed flutter margin moves downstream along the blade with increasing the inlet pressure, also at higher inlet pressures flutter stability reduces and the undesired vibration phenomena are more probable because of increased shock strength.

Additionally, FSI simulations for 5 blade profiles with different thickness distribution have been performed and the effect of fluid behaviour on the stability is investigated. The results show that in profiles with thinner trailing edge radius, the flutter margin is pronounced. Furthermore, it has been observed that the leading-edge radius and t_{max} increase the flutter instability but have less effects on the stability margin in comparison with trailing edge radius. It is noted that the experimental study of the effects of blade profiles on the flutter margin will be conducted as the next step in future studies.

Declaration of Competing Interest

The authors declare that they have no known competing financial interests or personal relationships that could have appeared to influence the work reported in this paper.

References

[1] D. Vogt, Experimental investigation of three-dimensional mechanisms in low-pressure turbine flutter. PhD Thesis, Royal Institute of Technology, Department of Heat and Power Technology, Stockholm, Sweden, 2005.
[2] J.G. Marshall, M. Imregun, A review of aeroelasticity methods with emphasis on turbomachinery applications, J. Fluids Struct. 10 (3) (1996) 237–267.
[3] A.V. Srinivasan, Flutter and resonant vibration characteristics of engine blades, ASME J. Eng. Gas Turbines Power 119 (1997) 742–775.
[4] O. Bendiksen, P. Friedman, Coupled bending-torsion flutter in a supersonic cascade, AIAA, 1980.
[5] H. Forsching, A parametric study of the flutter stability of two-dimensional turbine and compressor cascades in incompressible flow, Zeitschrift fur Flugwissenschaften and Weltraumforschung 13 (1989) 351–364.
[6] J. Panovsky, R.E. Kielb, A design method to prevent low pressure turbine blade flutter, Trans. ASME 122 (1) (2000) 89–98.
[7] M.D. Montgomery, J.M. Verdon, A three-dimensional linearized unsteady Euler analysis for turbomachinery blade rows. Contractor Report 4770, Natl. Aeronaut. Space Admin. (1997).
[8] F. Poli, E. Gambini, A. Arnone, C. Schipani, A three-dimensional time-linearized method for turbomachinery blade flutter analysis. Proceedings of the 11th International Symposium of Unsteady Aerodynamics Aeroacoustics and Aeroelasticity of Turbomachines, 2006.
[9] R. Rzadkowski, V. Gnesin, L. Kolodyazhnaya, 3D viscous flutter in turbomachinery cascade by Godunov-Kolgan method, Proceed. ASME Turbo Expo (2006). GT2006-90157.
[10] W.S. Clark, K.C. Hall, A time-linearized Navier-Stokes analysis of stall flutter, J. Turbomach. 122 (2000) 467–476.
[11] M.H. Hansen, Aeroelastic instability problems for wind turbines, Wind Energy 10 (6) (2007) 551–577.
[12] R.F. Ganiev, O.B. Balaksh, B.G. Kukharenko, In the case of turbocharger rotor blade flutter, J. Mach. Manuf. Reliab. 42 (1) (2013) 1–6.
[13] B.K. Kestner, J.S. Schutte, J.C. Gladin, D.N. Mavris, Ultra high bypass ratio engine sizing and cycle selection study for a subsonic commercial aircraft in the N+ 2 timeframe, Proceed. ASME Turbo Expo 610 (2011).
[14] E. Camara, Validation of time domain flutter prediction tool with experimental results, Energy Technol. EGI (2015), 011 EKV1081.
[15] S. Iseni, D. Micallef, R. Mailach, Investigation of inlet distortion on the flutter stability of a highly loaded transonic fan rotor, Proc. ASME Turbo Expo Turbomach. Tech. Conf. Expos. 7B (2016) 13–17, https://doi.org/10.1115/GT2016-56593.
[16] C. Ma, Z. Huang, M. Qi, Investigation on the forced response of a radial turbine under aerodynamic excitations, J. Therm. Sci. 25 (2) (2016) 130–137.
[17] L.i. He, Method of simulating unsteady turbomachinery flows with multiple perturbations, AIAA J. 30 (11) (1992) 2730–2735.
[18] J.I. Erdos, E. Alzner, Computation of unsteady transonic flows through rotating and stationary cascades, NASA (1978) Cr-2900.
[19] F. Lottinia, F. Poli, L. Pinelli, F. Vanti, R. Pacciani, Flutter stability assessment of a low pressure turbine rotor: A comparison between cantilever and interlocked configurations, AIP Conf. Proc. (2019), https://doi.org/10.1063/1.5138835.
[20] G.A. Gerolymos, Analysis and application of chorochronic periodicity for turbomachinery rotor/stator interaction computations, J. Propul. Power 18 (6) (2002) 1139–1152.
[21] D. Japikse, N.C. Baines, Introduction to turbo machinery, Norwich VT and Oxford UK Concepts ETI (1994).
[22] C. Copeland, The evaluation of steady and pulsating flow performance of a double-entry turbocharger turbine, University of London, UK, 2010. PhD Thesis.
[23] M. Schwitzke, A Schulz, H. Bauer, Prediction of high-frequency blade vibration amplitudes in a radial inflow turbine with nozzle guide vanes. Proceedings of ASME Turbo Expo, Turbine Technical Conference and Exposition, paper no. GT 2013, Texas, USA.
[24] D. Micallef, D. Witteck, A. Wiedermann, Three-dimensional viscous flutter analyses of a turbine cascade in subsonic and transonic flows, Proc. ASME Turbo Expo paper no. GT2012-68396 (2012).